A giant radio flare from Cygnus X-3 with associated γ-ray emission

S. Corbel, G. Dubus, J. A. Tomsick, A. Szostek, R. H. D. Corbet, J. C. A.
Miller-Jones, J. L. Richards, G. Pooley, S. Trushkin, R. Dubois, et al.

A giant radio flare from Cygnus X-3 with associated γ-ray emission

S. Corbel,[1,2]★ G. Dubus,[3] J. A. Tomsick,[4] A. Szostek,[5,6] R. H. D. Corbet,[7,8]
J. C. A. Miller-Jones,[9] J. L. Richards,[10] G. Pooley,[11] S. Trushkin,[12] R. Dubois,[5]
A. B. Hill,[13] M. Kerr,[5] W. Max-Moerbeck,[10] A. C. S. Readhead,[10] A. Bodaghee,[4]
V. Tudose,[14] D. Parent,[15] J. Wilms[16] and K. Pottschmidt[7,17]

[1]*Université Paris 7 Denis Diderot and Service d'Astrophysique, UMR AIM, CEA Saclay, F-91191 Gif sur Yvette, France*
[2]*Institut Universitaire de France, 75005 Paris, France*
[3]*UJF-Grenoble 1 / CNRS-INSU, Institut de Planétologie et d'Astrophysique de Grenoble (IPAG) UMR 5274, Grenoble F-38041, France*
[4]*Space Sciences Laboratory, 7 Gauss Way, University of California, Berkeley, CA 94720-7450, USA*
[5]*Kavli Institute for Particle Astrophysics and Cosmology, Department of Physics and SLAC National Accelerator Laboratory, Stanford University, Stanford, CA 94305, USA*
[6]*Astronomical Observatory, Jagiellonian University, Orla 171, 30-244 Kraków, Poland*
[7]*CRESST and NASA Goddard Space Flight Center, Astrophysics Science Division, Code 662, Greenbelt, MD 20771, USA*
[8]*Center for Space Science and Technology, University of Maryland Baltimore County, 1000 Hilltop Circle, Baltimore, MD 21250, USA*
[9]*International Centre for Radio Astronomy Research - Curtin University, GPO Box U1987, Perth, WA 6845, Australia*
[10]*Cahill Center for Astronomy and Astrophysics, California Institute of Technology, Pasadena, CA 91125, USA*
[11]*Cavendish Laboratory, J. J. Thomson Avenue, Cambridge CB3 0HE*
[12]*Special Astrophysical Observatory RAS, Karachaevo-Cherkassian Republic, Nizhnij Arkhyz 369167, Russia*
[13]*School of Physics & Astronomy, University of Southampton, Highfield, Southampton SO17 1BJ*
[14]*Netherlands Institute for Radio Astronomy, Postbus 2, 7990 AA Dwingeloo, the Netherlands*
[15]*Center for Earth Observing and Space Research, College of Science, George Mason University, Fairfax, VA 22030, resident at Naval Research Laboratory, Washington, DC 20375, USA*
[16]*Erlangen Centre for Astroparticle Physics, D-91058 Erlangen, Germany*
[17]*CRESST and NASA Goddard Space Flight Center, Astrophysics Science Division, Code 661, Greenbelt, MD 20771, USA*

ABSTRACT

With frequent flaring activity of its relativistic jets, Cygnus X-3 (Cyg X-3) is one of the most active microquasars and is the only Galactic black hole candidate with confirmed high-energy γ-ray emission, thanks to detections by *Fermi* Large Area Telescope (*Fermi*/LAT) and *AGILE*. In 2011, Cyg X-3 was observed to transit to a soft X-ray state, which is known to be associated with high-energy γ-ray emission. We present the results of a multiwavelength campaign covering a quenched state, when radio emission from Cyg X-3 is at its weakest and the X-ray spectrum is very soft. A giant ($\sim$20 Jy) optically thin radio flare marks the end of the quenched state, accompanied by rising non-thermal hard X-rays. *Fermi*/LAT observations ($E \geq 100$ MeV) reveal renewed γ-ray activity associated with this giant radio flare, suggesting a common origin for all non-thermal components. In addition, current observations unambiguously show that the γ-ray emission is not exclusively related to the rare giant radio flares. A three-week period of γ-ray emission is also detected when Cyg X-3 was weakly flaring in radio, right before transition to the radio quenched state. No γ-rays are observed during the $\sim$1-month long quenched state, when the radio flux is weakest. Our results suggest transitions into and out of the ultrasoft X-ray (radio-quenched) state trigger γ-ray emission, implying a connection to the accretion process, and also that the γ-ray activity is related to the level of radio flux (and possibly shock formation), strengthening the connection to the relativistic jets.

Key words: black hole physics – stars: individual: Cyg X-3 – ISM: jets and outflows – gamma-rays: stars – radio continuum: stars – X-rays: binaries.

★E-mail: stephane.corbel@cea.fr

1 INTRODUCTION

Galactic and extragalactic accreting systems containing a neutron star or a black hole can produce outflows containing energetic particles that are accelerated away from the compact object up to relativistic speeds in collimated jets. These high-energy particles, entangled in the jet magnetic field, lose their energy via synchrotron, inverse-Compton emission and/or adiabatic losses, or via pion production in the case of baryonic jets, resulting in a broad-band spectrum from radio up to high-energy γ-rays. (e.g. Atoyan & Aharonian 1999; Georganopoulos, Aharonian & Kirk 2002; Romero et al. 2003).

Cyg X-3 was one of the first sources to be discovered in the early days of X-ray astronomy (Giacconi et al. 1967). It is a system consisting of a Wolf–Rayet star (van Kerkwijk et al. 1992) and a compact object (most likely a black hole). With a short 4.8-h orbital period (Parsignault et al. 1972), Cyg X-3 lies at a distance of the order of ~7 kpc (Ling, Zhang & Tang 2009). The X-ray spectrum from Cyg X-3 changes between hard and soft states akin to those observed in other accreting X-ray binaries, and is heavily absorbed at low energies by the intervening dense stellar wind (Szostek, Zdziarski & McCollough 2008; Hjalmarsdotter et al. 2009). Cyg X-3 is also known for the recurrent activity of its relativistic jets that make it one of the brightest Galactic transient radio sources (e.g. Mioduszewski et al. 2001; Miller-Jones et al. 2004).

AGILE and *Fermi* Large Area Telescope (*Fermi*/LAT) reported concurrent detections of Cyg X-3 in high-energy γ-rays (>100 MeV), closely related to the activity of the relativistic jet during the soft X-ray state (Tavani et al. 2009; Fermi LAT Collaboration et al. 2009, hereafter FLC09). The γ-ray emission measured by the *Fermi*/LAT was found to be modulated on the orbital period, securing the identification (FLC09). A very short γ-ray flare was reported later during a short transient softening of Cyg X-3 in 2010 (Bulgarelli et al. 2010; Corbel & Hays 2010; Williams et al. 2011). No evidence for emission above 250 GeV has been found by MAGIC (Major Atmospheric Gamma-ray Imaging Cherenkov Telescope; Aleksić et al. 2010).

Cyg X-3 is the first binary hosting an accreting compact object and relativistic jet (also known as microquasar) to be detected in γ-rays. It is clearly an accreting source unlike γ-ray binaries that are more naturally explained by pulsar spin-down power (Dubus 2006). The nature and location of the non-thermal processes that bring particles to high energies, the relationship between these processes, jet launching and accretion state are long-standing questions for both microquasars and active galactic nuclei that stand to benefit from this detection. In Cyg X-3, jet emission can be followed and resolved spatially in radio, the accretion state is traced by the X-rays while the newly detected γ-rays provide a window into particle acceleration. In early 2011, Cyg X-3 underwent a new transition to the soft state (Kotani et al. 2011b), which was accompanied by transient γ-ray emission detected by *AGILE* and *Fermi* (Bulgarelli et al. 2011a,b; Corbel et al. 2011). The transition was monitored in radio, γ-rays, soft and hard X-rays (Section 2). The *Fermi*/LAT detections occurred exactly prior to and following a period of quenched radio emission and ultrasoft/hypersoft X-ray emission (Section 3). The LAT detection accompanying a major radio flare casts new light on the relationship between non-thermal radio, X-ray and γ-ray emission and relativistic ejection (Section 4).

2 OBSERVATIONS AND DATA ANALYSIS

Cyg X-3 is continuously monitored in γ-ray, soft and hard X-ray by all-sky monitors like *Fermi*/LAT, the *Monitor of All-sky*

X-ray Image (*MAXI*), the All-Sky Monitor aboard the *Rossi X-ray Timing Explorer* (*RXTE*/ASM) and the Burst Alert Telescope on the *Swift* mission (*Swift*/BAT). Dedicated radio observations are also frequently conducted to constrain the variable activity of its relativistic jets.

2.1 γ-ray

We present the results of observations of the Cygnus region with the *Fermi*/LAT (Atwood et al. 2009) along the course of its recent 2011 active phase. The reduction and analysis of LAT data were performed using Science Tools v.9.24. LAT photons within a 15° acceptance cone centred on the location of Cyg X-3 were selected in the energy range from 100 MeV to 100 GeV. To minimize contamination by Earth albedo photons, γ-ray events that have reconstructed directions with angles with respect to the local zenith >100° have been excluded. The rocking angles were restricted to <52°. Due to the potential contamination of the nearby pulsar PSR J2032+4127 (~30 arcmin from Cyg X-3), we used its most up-to-date ephemeris[1] to select the LAT data from its off-pulse phase intervals (removing only ~19 per cent of the useful exposure). The instrument response functions (IRFs) 'P6_V11_DIFFUSE' have been used throughout this paper.

Aiming to construct a light curve on ~ daily time-scales, we first characterized the sources within this crowded field of view (e.g. FLC09) by using the *Fermi* data over the 2-yr period with an internal source list made under IRFs 'P6_V11_DIFFUSE' and different spectral models. A binned maximum-likelihood spectral analysis was then performed to further constrain the spectral parameters of the sources within 3° (with all free parameters) and 9° (with only the normalization free) from Cyg X-3. The two nearby bright pulsars (PSR J2021+4026 and PSR J2021+3651) were modelled with an exponentially cut-off power-law model with all parameters let free to vary. We included models for the Galactic diffuse emission (gll_iem_v02) and an isotropic component (isotropic_iem_v02) including the extragalactic diffuse emission and the residual background from cosmic rays. Both diffuse components were renormalized for use under IRFs 'P6_V11_DIFFUSE'.

Once the spectral parameters of the sources in the field of view were fully characterized, we fixed those parameters and performed an unbinned maximum-likelihood analysis on different time-scales ranging from 6 h to 4 d. In this procedure, the remaining free parameters are the normalization of the Galactic diffuse emission and the normalization of the power law that is used to model Cyg X-3 (as described in FLC09). In time bins where Cyg X-3 is not detected, which we take to correspond to a test statistic, TS < 20 (4-d bin) or TS < 9 (shorter time bins), a 95 per cent confidence upper limit is calculated. The upper limit is calculated using the Bayesian method of Helene (1991), as implemented in the Python UPPER LIMITS module provided with the *Fermi* Science Tools, with the Cyg X-3 power-law photon index fixed to be 2.7.

Following the reactivation of Cyg X-3 in γ-rays (Corbel et al. 2011), a dedicated target of opportunity (ToO) observation was also conducted by *Fermi*/LAT starting on 2011 March 24 (MJD 55644.65). However, the end of the flaring activity of Cyg X-3 resulted in an termination of the ToO observation on March 28 (MJD 55648.63).

---

[1] LAT pulsar timing models available here: https://confluence.slac.stanford.edu/display/GLAMCOG/LAT+Gamma-ray+Pulsar+Timing+Models.

2.2 Radio

Since the launch of *Fermi* in 2008 June, we have had an ongoing monitoring programme of Galactic binaries with the Owens Valley Radio Observatory (OVRO) 40-m single-dish telescope located in California (USA). The OVRO flux densities are measured in a single 3-GHz band centred on 15 GHz using Dicke switching and dual-beam sky switching to remove atmospheric interference. The Galactic binaries sample, including Cyg X-3, is observed with the same cadence and procedures used for the blazar monitoring programme described in Richards et al. (2011). In addition, two days of intensive monitoring of Cyg X-3 were performed while the source was above the OVRO horizon in 2011 February (MJD 55599 and 55601). An offset of 0.124 Jy has been removed from the OVRO flux densities to account for the effect of extended nearby sources (Sánchez-Sutil et al. 2008) that are usually resolved out by interferometers (based on a comparison with AMI (Arcminute Microkelvin Imager) data obtained simultaneously at the same frequency; FLC09).

We take advantage of the large set of measurements provided by the AMI Large array (Cambridge, UK), consisting of a set of eight 13-m antennas with a maximum baseline of ∼120 m. AMI observations are conducted with a 6-GHz bandwidth centred at 15 GHz (Zwart et al. 2008). We also used the 11.2-GHz data of Cyg X-3 from a monitoring programme (Trushkin et al. 2006) with the RATAN-600 telescope located near Zelenchurskaya village on the North Caucas (Russia). Its 11.2-GHz radiometer is cooled by the cryogenic system up to 12 K. No frequency correction has been applied to the RATAN data.

2.3 X-ray

We used the one day average quick-look measurements in soft and hard X-rays from (1) *RXTE*/ASM (1.5–12 keV; Levine et al. 1996),

(2) *MAXI* (1.5–20 keV; Matsuoka et al. 2009) installed on the International Space Station and (3) *Swift*/BAT (15–50 keV; Barthelmy et al. 2005).

We also obtained pointed *RXTE* observations between 2011 February 19 (MJD 55611) and 2011 April 4 (MJD 55655). The 46 approximately daily monitoring observations performed under this programme (P96375) were triggered by Cyg X-3 entering the ultrasoft X-ray/quenched radio state, and we followed the evolution of the Cyg X-3 X-ray properties as the source made its expected transition out of this state. We extracted the Proportional Counter Array (PCA; Jahoda et al. 2006) data from these observations, and the source evolution is characterized in terms of the hardness ratio and the detailed spectral properties below. The average PCA exposure time per observation is ∼2.7 ks.

We produced 3–50 keV PCA energy spectra for the 46 *RXTE* observations. We used the standard tools provided in HEASOFT v6.11 to produce source and background spectra and included the recommended 0.5 per cent systematic uncertainties. We carried out the spectral fits with the XSPEC v12 software package. As the spectrum varies with the orbital modulation, we restricted our analysis to the observations obtained near the peak of the modulation. Table 1 lists the five observations for which we carried out spectral fits along with their orbital phases. The first of these observations occurred when the source was still in the ultrasoft state and the last was after the γ-ray flare and during the decay of the radio flare.

We also used the *RXTE*/PCA data to characterize the Cyg X-3 X-ray timing properties during the five observations for which we reported detailed spectral properties above. We made light curves from the 'Standard 1' data, which have 0.125 s time resolution and effectively no energy resolution. The single energy bin includes all PCA channels, corresponding to an energy band of ∼2–60 keV. We first produced 0.002–4 Hz power spectra in the Leahy et al. (1983) normalization and then subtracted the Poisson noise level and divided by the total count rate to convert to

Table 1. Main spectral parameters (according to their definitions in eqpair; see Hjalmarsdotter et al. 2009) from the best-fitting models of the five *RXTE* spectra discussed in Section 4 and Fig. 4. The eqpair parameters are as follows: l_h/l_s defines the ratio of the hard to soft compactness, kT_{bb} is the temperature of the inner edge of the accretion disc, l_{nt}/l_h corresponds to the fraction of power supplied to the energetic particles which goes into accelerating non-thermal particles, τ_p is the thermal plasma optical depth and Γ_{inj} is the index of the power law of the accelerated non-thermal electrons. For the timing section in the bottom of the table, we report the power-law index α used in the fitting of the PDS (see Fig. 5) along with the rms amplitude (in per cent) of the variability in the 0.002–0.1 Hz range. The quoted uncertainties correspond to 90 per cent confidence.

Parameter	Spectrum 1	Spectrum 2	Spectrum 3	Spectrum 4	Spectrum 5
			Spectral and timing parameters for the five *RXTE* observations of Cyg X-3		
ObsID	29-00	32-00	33-00	36-00	40-00
MJD−55000	639.0	642.0	643.0	646.0	649.8
Orbital phase	0.46–0.65	0.51–0.64	0.41–0.60	0.46–0.65	0.43–0.60
Spectral					
l_h/l_s	$0.15^{+0.05}_{-0.01}$	$0.28^{+0.08}_{-0.05}$	$0.018^{+0.008}_{-0.005}$	$0.061^{+0.007}_{-0.009}$	0.034 ± 0.016
kT_{bb} (eV)	319^{+254}_{-91}	291^{+189}_{-91}	247^{+12}_{-22}	285^{+18}_{-41}	257^{+15}_{-35}
l_{nt}/l_h	$<9 \times 10^{-4}$	$0.013^{+0.002}_{-0.003}$	$0.22^{+0.01}_{-0.03}$	$0.44^{+0.26}_{-0.12}$	$0.996^{+0.004}_{-0.500}$
τ_p	$3.6^{+1.0}_{-0.1}$	$7.7^{+1.7}_{-1.0}$	$0.026^{+0.008}_{-0.001}$	$0.049^{+0.009}_{-0.019}$	$0.030^{+0.069}_{-0.023}$
Γ_{inj}	$4.5^{+0.5}_{-4.5}$	$4.0^{+0.0}_{-1.1}$	$5.0^{+0.0}_{-0.5}$	$5.8^{+0.2}_{-0.3}$	$5.8^{+0.2}_{-0.2}$
χ^2/ν	78/62	57/62	52/63	61/62	46/62
Timing					
α	1.97 ± 0.20	$3.2^{+2.1}_{-0.9}$	2.7 ± 0.4	$2.29^{+0.13}_{-0.14}$	$2.14^{+0.24}_{-0.27}$
rms (per cent)	$2.21^{+0.02}_{-0.14}$	$0.75^{+0.01}_{-0.23}$	$1.73^{+0.02}_{-0.18}$	$3.73^{+0.13}_{-0.29}$	$2.09^{+0.12}_{-0.30}$

the rms power spectra (Miyamoto et al. 1991) that are shown in Fig. 5. We fitted the power spectra with a power-law model, and used these fits to determine the overall fractional rms level for each observation.

3 RESULTS

3.1 Radio and X-ray emission during the 2011 soft state

The long-term light curves of Cyg X-3 in soft and hard X-rays are presented in the two top panels of Fig. 1, along with the radio light curve in the bottom panel. The X-ray and radio states, as defined by Szostek et al. (2008), are marked on top of this figure. Up to mid-October 2010 (∼MJD 55480), Cyg X-3 is found in its typical hard state. At that time, *MAXI* and *RXTE*/ASM data show a rise in soft X-rays (≈2–5 keV), whereas *Swift*/BAT measures a decline in hard (>15 keV) X-rays, highlighting an initial transition to the soft/suppressed X-ray/radio state. The 3–5 keV count rate from the *RXTE*/ASM of ≈3 count s^{-1} corresponds to the pivotal value separating hard from predominantly soft X-ray states in Cyg X-3 (see fig. 6 of Szostek et al. 2008). The decrease (∼MJD 55500)

in soft X-ray flux indicates a temporary return to the level of the hard/soft state transition and minor flaring radio state. The further increase in soft X-rays above the pivotal ASM value starting from ≈MJD 55540 marks the full transition to the soft state, while the abrupt drop in hard X-ray flux on MJD 55608 (2011 February 16) indicates the transition to the ultrasoft X-ray state.

Once fully in the soft state, Cyg X-3 is again in the suppressed radio state (between MJD 55540 and 55570), and then the radio emission is variable with the presence of flares with peak flux densities reaching ∼0.6 Jy at 15 GHz. As opposed to the solitary major radio flares (>10 Jy), which are known to follow quenched radio states and to decay on time-scales of days, these small radio flares (<1 Jy) are shorter in duration, more rapidly variable and may occur in clusters of groups that are alternating with short periods of radio emission at the level typical of the suppressed radio state (a good example can be found in Miller-Jones et al. 2009). The small radio flaring activity was first named by Waltman et al. (1994) and was not included in the classification of X-ray and radio states of Szostek et al. (2008). Apparent superluminal expansion during two small flares, with peak flux up to 0.3 Jy at 15 GHz, was observed by Newell, Garrett & Spencer (1998). Furthermore, on several
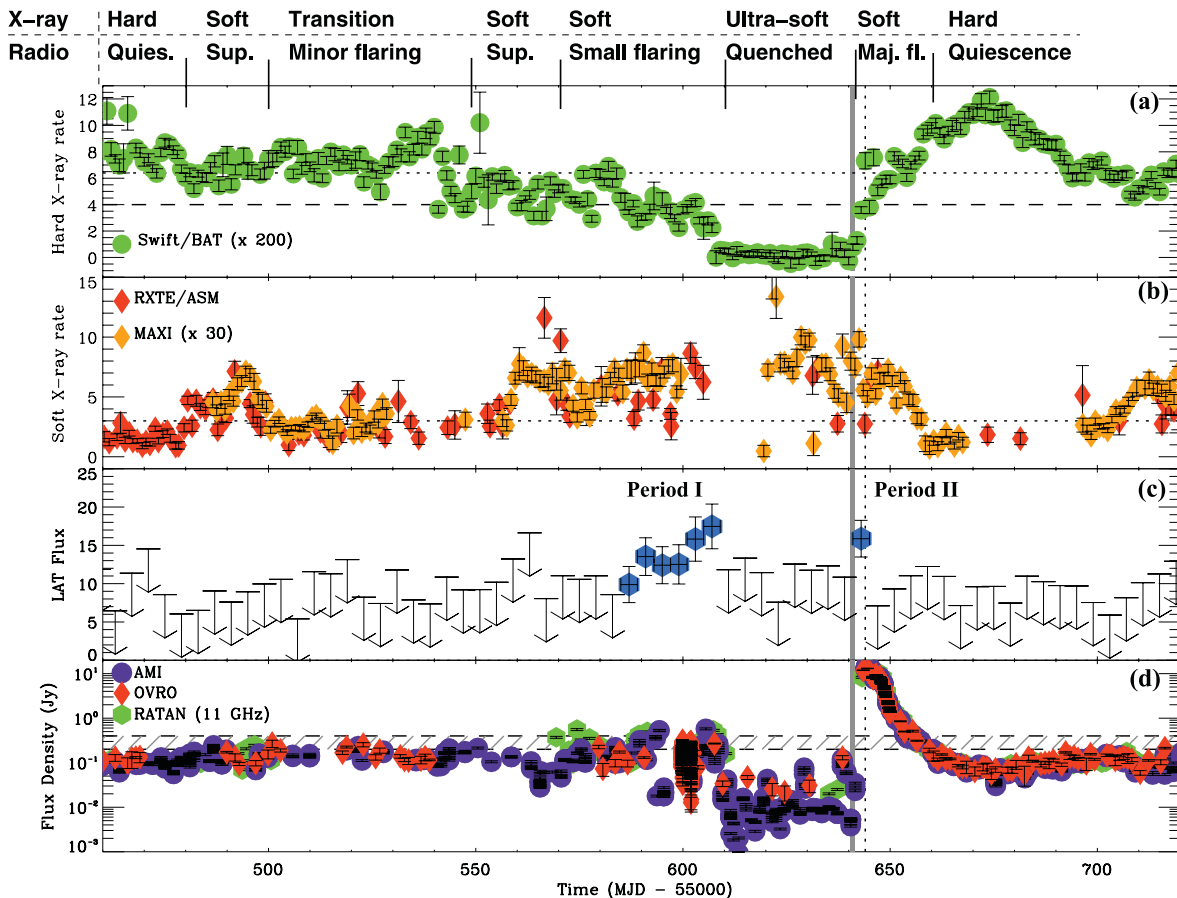

Figure 1. Hard X-ray light curve in panel (a) from *Swift*/BAT (15–50 keV; green) with the soft X-ray light curves in panel (b) from *RXTE*/ASM (3–5 keV; red) and *MAXI* (1.5–4 keV; orange) from 2010 September 21 to 2011 June 8. The horizontal dotted line in (a) and (b) highlights the emission level corresponding to the hard to soft state transition (e.g. the ASM 3–5 keV pivotal rate of 3 count s^{-1} of Szostek et al. 2008). Panel (c): LAT flux ($E \geq 100$ MeV) light curve of Cyg X-3 obtained in 4-d bins. The LAT fluxes (left axis) are expressed in units of 10^{-7} photon cm^{-2} s^{-1} above 100 MeV. LAT upper limits are represented at the 95 per cent confidence level. Panel (d): radio light curve of Cyg X-3 at 15 GHz based on the OVRO, AMI and RATAN (at 11.2 GHz) data. The onset of the giant radio flare is indicated in the four panels by the large vertical grey band, whereas the peak of this flare is marked with the vertical dotted line (see Fig. 3 for a zoom on this interval and Fig. 2 for period I). The horizontal dashed lines in panels (a) and (d) (and hatched area = the 0.2–0.4 Jy zone) highlight the thresholds (see discussion in paper) corresponding to the detection of γ-ray emission of Cyg X-3 by LAT. The labels in the top of the figure indicate the corresponding X-ray/radio state of Cyg X-3 ('Quies.', 'Sup.' and 'Maj. fl.' stand respectively for 'quiescence', 'suppressed' and 'major flaring' radio state).

occasions these small flares have been observed up to the millimetre domain, which was also occasionally the case early in 2011 with inverted spectra up to 98 GHz (e.g. Kotani et al. 2011a; S. Trushkin, private communication), suggesting temporary optically thick synchrotron emission. All these radio properties are consistent with Cyg X-3 moving in early 2011 from the suppressed state to a state of small flaring radio activity.

The time span between MJD 55610 and 55640 with weak radio emission (down to 2 mJy) and very low hard X-ray emission is characteristic of the quenched radio state that always precedes a giant flare (Waltman et al. 1994; Fender et al. 1997). Cyg X-3 is then in its ultrasoft (Szostek et al. 2008; Koljonen et al. 2010) X-ray spectral state characterized by strong thermal soft X-rays and a very weak or absent non-thermal power law in hard X-rays. Optically thick radio spectra are usually observed in this state (Waltman et al. 1995).

The giant radio flare that ends the quenched state reached a flux of almost 20 Jy at 15 GHz (Corbel et al. 2011). Fig. 3 highlights the rising part of this flare, indicating a likely onset (defined by the gradual increase of radio emission at the end of the quenched radio state) around MJD 55641.0 ±0.5 and peak flux around MJD 55644 (also marked in Fig. 1). The delay between onset and peak is consistent with observations during previous giant radio flares (of the order of 2–4 d; e.g. Waltman et al. 1995; Miller-Jones et al. 2004). We caution that the exact trigger time of this relativistic ejection event could possibly occur after, or even before, the radio onset we highlighted above. Alternatively, the detection of a non-thermal X-ray component by *RXTE*/PCA on MJD 55642.0 (Fig. 4, Table 1 and Section 4.2) and the hardening of the X-ray spectra (Fig. 3) may also signal the trigger time of the ejection event (indicated in Fig. 3). The precise ejection date should be better constrained with the very long baseline interferometry (VLBI) campaign we conducted during this flare (Miller-Jones et al., in preparation).

The hard X-rays switch back on and are correlated with the radio flux during major flares (Szostek et al. 2008). The *RXTE*/PCA hardness ratio (Fig. 3) confirms the hardening, as well as the appearance of a hard X-ray tail in the *RXTE*/PCA spectra (see also Fig. 4 and discussion in Section 4.2) during the onset of the flare. This hard X-ray tail was not present during the radio quenched period of the 2011 soft state (Figs 1 and 4). The spectra during major radio flares typically show a non-thermal power law in hard X-rays (Szostek et al. 2008; Koljonen et al. 2010) and optically thin radio emission (Waltman et al. 1995).

3.2 Flaring γ-ray emission from Cyg X-3

The *Fermi*/LAT γ-ray light curve (0.1–100 GeV) with 4-d time bins is presented in panel (c) of Fig. 1. Only the very significant data points with test statistic (Mattox et al. 1996) TS ≥ 20 (∼4.5σ) are plotted, otherwise they are represented as upper limits. Two distinct phases of γ-ray activity are found: (1) a long phase (∼3 weeks) of γ-ray activity just before the ultrasoft state (hereafter period I); (2) a shorter γ-ray active phase (≤5 d) in conjunction with the giant radio flare (hereafter period II). No γ-ray emission is detected during the quenched radio state in between period I and II, corresponding to the ultrasoft X-ray state.

Regarding period I (see also zoom-in Fig. 2), we note that the 4-d bin data (from MJD 55585 to 55610) are consistent with a steady increase of γ-ray emission up to a flux (≥100 MeV) ∼1.8 × 10^{-6} photon cm^{-2} s^{-1}, just before transition to the quenched radio state. However, the data on shorter bins (Fig. 2) indicate variability on time-scales as short as 1 d. γ-ray emission in period I occurs after the soft X-ray emission has increased beyond the ASM pivotal value (∼3 count s^{-1}), also during a significant decrease in hard X rays (BAT flux ≲ 0.02 count cm^{-2} s^{-1}) and in a period of short and faint radio flaring, placing Cyg X-3 in the small flaring radio
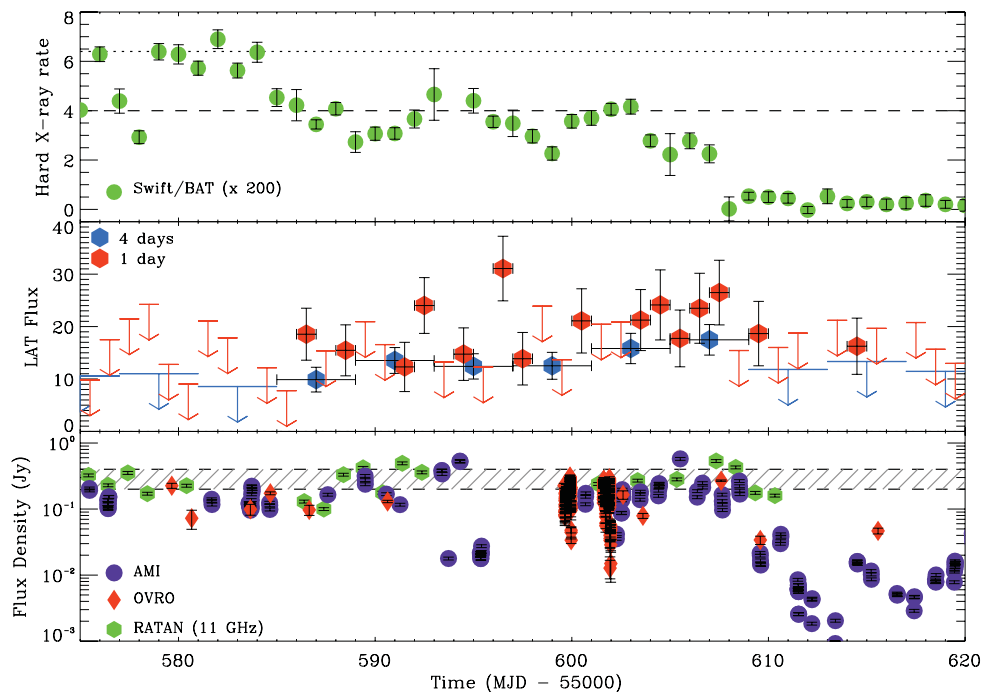

Figure 2. Same as Fig. 1 but for a time interval around period I (2010 December 30 to 2011 February 28). The soft X-rays (not shown for clarity) were all above the ASM pivotal value of 3 count s^{-1}. The LAT fluxes in 1-d time bin are also plotted in the middle panel.
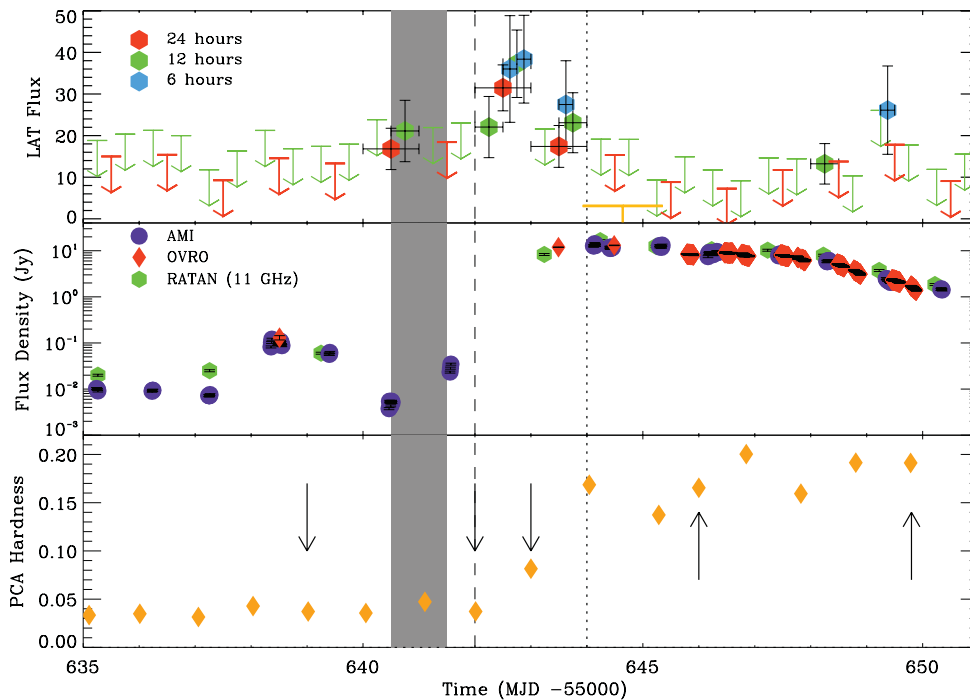
Figure 3. Top panel: LAT flux ($E \geq 100$ MeV) light curve of Cyg X-3 obtained in 1-d, 12- and 6-h bins for the period around the giant radio flare (2011 March 15–31). The orange upper limit corresponds to the 95 per cent confidence upper limit during the *Fermi* ToO observations. Middle panel: radio light curve (same data as Fig. 1, including AMI, OVRO and RATAN) of Cyg X-3 highlighting the onset of the giant radio flare that gives a starting date for the radio flare of MJD $\sim 55641.0 \pm 0.5$. Bottom panel: evolution of the *RXTE*/PCA hardness ratio (defined as count rate in band 10–50 keV over band 3–10 keV). The error bars are smaller than the symbol size. The arrows indicate the time of the five *RXTE* spectra discussed in Section 4.2 and Fig. 4. For all panels, the onset of the giant radio flare is indicated by the large vertical grey band (based on the increase in radio flux density) or the vertical dashed line (based on the appearance of a non-thermal X-ray component), whereas the peak of this flare is marked with the vertical dotted line.

state (as discussed in Section 3.1). The *AGILE* collaboration also reported detections of Cyg X-3 during period I (Bulgarelli et al. 2011a,b). No pointed *RXTE* observations were executed in period I, and therefore we cannot determine if a non-thermal hard X-ray tail was present during that time, as we do below for period II.

For period II, we constructed LAT light curves on 6-h, 12-h and 1-d intervals to highlight the onset of the γ-ray emission and to allow a comparison with the giant radio flare. Due to the shorter integration time, only data points with TS > 9 ($\sim 3\sigma$) are plotted (otherwise, they are represented as upper limits) in Fig. 3. The short γ-ray activity in period II occurs during the rise of the radio flare. The γ-ray emission turns off before the peak of radio emission (vertical dotted line in Fig. 3). The first LAT detection occurs on MJD 55640.5 ± 0.5, implying a γ-ray turn-on consistent with the exact onset of the radio flare defined by the increase in radio flux density (illustrated by the grey area in Fig. 3; see also Section 3.1). Based on the 6- and 12-h bin light curves, the peak in γ-rays (≈ 3–4×10^{-6} photon cm^{-2} s^{-1}) is reached on MJD 55642.75 ± 0.25, which is well before (by 1.5 d) the peak flux in radio. Short time-scale variability might be present within this active phase: the LAT 1-d bin on MJD 55641.5 ± 0.5 is consistent with a non-detection although there is no significant change in LAT exposure towards Cyg X-3 on this specific day. This would be consistent with the upper limits reported by *AGILE* around this time (Bulgarelli et al. 2011c). Furthermore, we note that most of the LAT detections occur after the onset of the non-thermal X-ray component (illustrated by the dashed line in Fig. 3; see also Section 3.1). *Fermi* conducted a dedicated ToO observation from MJD 55644.65 to 55648.63 with no detection of Cyg X-3. We derived a 95 per cent LAT flux (≥ 100 MeV) upper

limit of 3.1×10^{-7} photon cm^{-2} s^{-1} for the ToO interval, implying a reduction of the γ-ray emission by more than a factor 10 on a time-scale of a few days. Furthermore, we find no significant detection by the LAT at the time of the other detection reported by *AGILE* (Piano et al. 2011b) on MJD 55710.

Integrating the LAT data separately over the two flaring periods results in photon indices ~ 2.5–2.7 consistent with the previously published LAT spectra (FLC09). Furthermore, modulation of the γ-ray emission at the orbital period of Cyg X-3 (FLC09) is again detected by *Fermi*/LAT in both epochs; but the short duration of the present activity prevents a detailed analysis and will be investigated in a subsequent study using Pass 7 IRFs[2] which have increased effective area at low energies.

4 DISCUSSION

4.1 Conditions for detection of high-energy γ-ray emission from Cyg X-3

High-energy γ-ray emission has now been reported by *Fermi*/LAT at four different epochs (2008 October/December, 2009 June/July, 2010 May, 2011 March). In all cases the LAT detections were contemporaneous, but not coincident, with the hard X-ray light curve crossing a threshold level, i.e. *Swift*/BAT count rates of 0.02 count cm^{-2} s^{-1} (if only for a day in 2010; Williams et al.

2011). In period I, the crossing proceeded from higher to lower flux, whereas in period II it was in the opposite direction. The *RXTE*/ASM flux in the 3–5 keV band was also always at or above the pivotal value of 3 count s^{-1} that separates the canonical hard and soft X-ray states of Cyg X-3 (Szostek et al. 2008; Koljonen et al. 2010). These conditions on the X-ray fluxes appear necessary to detect γ-ray emission (see also Piano et al. 2011a, for the *AGILE* detections).

When its X-ray spectrum is predominantly soft, Cyg X-3 can be found in a suppressed, quenched, small or major flaring state depending on the behaviour in radio. The 2008–09 detections and the new LAT detection in period II occurred during major flaring activity, with radio fluxes in excess of a few Jy and optically thin spectra. The new LAT detection in period I occurred at a time when Cyg X-3 was most likely moving through a series of small radio flares, with 15-GHz flux densities ≈0.1–0.6 Jy. The radio and X-ray conditions during the brief γ-ray detection of 2010 May (Williams et al. 2011) appear similar to those of period I. We do not detect γ-ray emission during the quenched radio state, when the radio emission is very low and the X-ray spectrum is ultrasoft. However, we cannot exclude that very faint γ-ray emission (at least much below the sensitivity of LAT) could eventually be present in this state, as the radio light curve (Fig. 1) indicate some variability from the jets. We also note that γ-rays are not present in the mid- to later stages of period II, even though the radio emission is still very bright (>1 Jy). Slowly decaying jets are not associated with γ-ray emission, and consequently a rapid rise in radio emission (possibly caused by strong shocks, see Section 4.3), up to at least ≈0.2–0.4 Jy, may therefore be required.

Hence, the level of γ-ray emission depends also on the presence of radio emission at a level greater than ≈0.2–0.4 Jy, reinforcing the association of γ-ray activity with the significant emission from the relativistic jets. In other words, particle acceleration to very high energies does not happen exclusively during rare major radio flares but a relatively low level radio activity suffices. To summarize, three conditions seem to be required in order to detect significant high-energy γ-ray emission from Cyg X-3: (1) a high level of soft X-ray emission (the 3–5 keV *RXTE*/ASM value above 3 count s^{-1}, i.e. Cyg X-3 needs to be in the soft state), (2) a low level of hard X-ray emission (*Swift*/BAT below 0.02 count cm^{-2} s^{-1}) and (3) the presence of significant emission with rapid variation from active relativistic jets (with 15-GHz radio flux above ≈0.2–0.4 Jy). However, γ-ray emission can temporarily be seen at lower radio fluxes (e.g. onset of emission during epoch II), and therefore a comprehensive picture taking into account possible delays or binning will be examined in future work. Furthermore, it is unclear at present how the shape of the radio spectrum (optically thin or thick synchrotron emission) relates to the γ-ray emission.

4.2 A non-thermal X-ray component during the giant radio flare

Giant radio flares start in the ultrasoft X-ray state, which also shows a rising non-thermal component beyond 15 keV while the soft thermal emission remains steady (e.g. Szostek et al. 2008). The *RXTE*/PCA spectra during the transition (Fig. 4) confirm the appearance of a hard X-ray tail during the onset of the flare in period II. The 2011 March giant radio flare shows that the simultaneous rise in non-thermal radio and hard X-ray components also involves high-energy γ-ray emission. One of the *RXTE*/PCA observations occurred on MJD 55643 (spectrum 3 in Fig. 4 and Table 1) while the source was being detected in the γ-ray band by LAT. Due to the
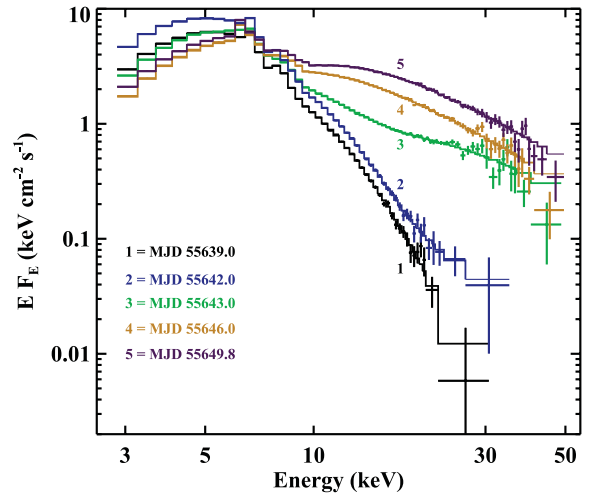

Figure 4. *RXTE*/PCA spectra during the soft to hard state transition associated with the giant radio flare of Cyg X-3 in 2011. They correspond to the periods: before the onset of the radio and γ-ray flare (spectrum 1 on MJD 55639), (2) the onset of the γ-ray flare (spectrum 2 on MJD 55642), (3) the peak of the γ-ray flare (spectrum 3 on MJD 55643) and (4) after the peak of the radio flare (spectra 4 and 5). For illustrative purposes, adjacent bins have been grouped until they reach a significant detection of at least 3σ, but with a maximum of 10 bins combined.

complicated shape of the X-ray spectrum, the extrapolation from the X-ray to the γ-ray band is not straightforward. However, a rough estimate can be made by re-fitting the 10–50 keV portion of the PCA spectrum with a power law. The value of the best-fitting photon index is Γ = 3.4, and an extrapolation to >100 MeV predicts a flux of 1.0×10^{-11} photon cm^{-2} s^{-1}. This is several orders of magnitude lower than the measured LAT flux, indicating that the X-rays and γ-rays cannot be part of the same power law (even if the two emission regimes could still be connected) and that a spectral break is located between ∼100 keV and 100 MeV (see also Zdziarski et al. 2012). If the hard X rays and γ-rays are due to the same radiative process and generated at the same location, then the orbital modulation at both frequencies should be in phase.

It is well known that Cyg X-3 has a highly complex X-ray spectrum, and, as expected, simple models such as a power law, a power law with a cut-off, or thermal Comptonization (all with simple absorption) provide very poor fits. Thus, we used a model that has previously been used for Cyg X-3 (Szostek & Zdziarski 2008; Hjalmarsdotter et al. 2009), which is based on the `eqpair` hybrid thermal/non-thermal Comptonization model (Coppi 1992, 1999). In addition to `eqpair`, we included absorption with partial covering with two separate values of N_H and iron features (a broad line, a narrow line and an edge) as described in Hjalmarsdotter et al. (2009). As shown by the χ^2 values in Table 1, this model provided acceptable fits.

The `eqpair` parameters from the fits to the X-ray spectra are given in Table 1. Whereas the purpose of this work is not to do detailed spectral modelling (e.g. see Szostek & Zdziarski 2008; Hjalmarsdotter et al. 2009), this information can be used to provide some insights into the evolution of the X-ray spectra during the major radio flare (period II). However, as we do not have X-ray data below 3 keV, several degeneracies within the `eqpair` model (e.g. the hydrogen column density and the inner accretion disc temperature) cannot be removed. Whereas the model provides good fits to the data; the values reported in Table 1 should not be over-interpreted.
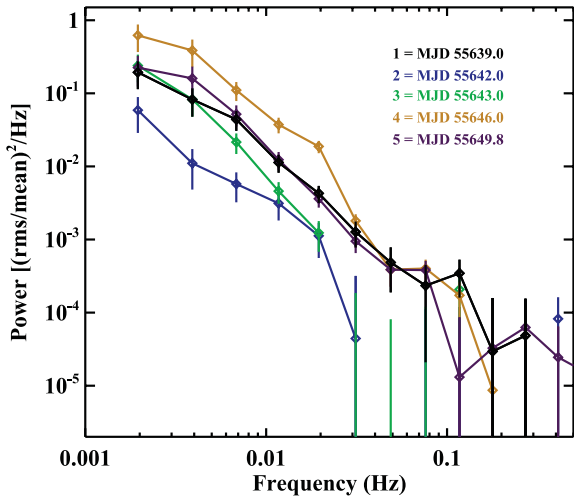
Figure 5. *RXTE*/PCA PDS during the soft to hard state transition (same dates and colours as in Fig. 4).

The solutions we obtained are in the regime of low seed photon temperature kT_{bb}, very soft electron injection spectrum Γ_{inj} and low plasma optical depth τ_p. Within this regime, one trend that is notable is the gradual increase in the l_{nt}/l_h parameter. This appears to be an indication of the increasing importance of non-thermal Comptonization in the spectrum as Cyg X-3 leaves the ultrasoft state. It is not clear how this is related to the γ-ray emission since the LAT detected Cyg X-3 only during the acquisition of spectrum 3, and this is not the spectrum with the largest non-thermal X-ray contribution (unless delayed emission is involved).

The power density spectra (PDS) corresponding to the five *RXTE*/PCA observations discussed above are plotted in Fig. 5. The PDS at frequencies higher than 10^{-3} Hz are well described by a power law with an index of ~ -2 (see the timing parameters in Table 1). No signal is detected above 0.1 Hz. The slope and rms noise levels of the PDS are similar to previous studies (Choudhury et al. 2004; Axelsson, Larsson & Hjalmarsdotter 2009). One noticeable difference can be seen in the power spectrum #2 with a lower noise level. This observation corresponds to the onset of non-thermal Comptonization as discussed in the previous paragraph. This lower variability may possibly be associated with a quiet accretion disc between the onset of the radio flare and the formation of the corona producing the hard X-ray emission.

4.3 Connecting the relativistic jets and the high-energy emission in Cyg X-3

A coherent picture of the link between accretion, ejection and the non-thermal emission we observe has yet to emerge. High levels of soft X-rays together with significant radio emission are related to the γ-ray activity, but the relative timings at the various wavelengths remain confusing: particle acceleration and cooling may lead to differing lags and peaks; correlations may also be blurred when multiple flares superpose. Rising soft X-ray emission is thought to accompany an increased accretion rate (perhaps due to variations in mass-loss rate from the Wolf–Rayet companion star; e.g. Gies et al. 2003) and a decreasing inner disc radius, eventually quenching the jet in the ultrasoft state (e.g. Hjalmarsdotter et al. 2009).

VLBI observations have shown that the variations in radio flux during major flares come from the resolved jet on milliarcsecond

($\geq$au) scales and not from the core (Tudose et al. 2010), raising the intriguing possibility that the non-thermal emission region is outside the binary system during major flares. However, there is no evidence yet that the radio emission is detached from the core during the *rising* phase of a major flare (when γ-ray emission was detected). Locating the high-energy electrons very far away (e.g. via VLBI observations) would place stringent constraints on jet parameters if the observed γ-ray modulation is due to inverse-Compton upscattering of photons from the Wolf–Rayet star (Dubus, Cerutti & Henri 2010; Sitarek & Bednarek 2012; Zdziarski et al. 2012).

A possible scenario is that the non-thermal emission is related to shocks forming at various distances along the jet, as previously suggested by modelling of the radio activity (Lindfors et al. 2007; Miller-Jones et al. 2009). Transitions in/out of the ultrasoft X-ray state then signal a decrease/increase in jet efficiency with the non-thermal region moving in/out. γ-ray emission may be most efficient at some 'sweet-spot' distance bounded by strong pair production on thermal X-rays (Cerutti et al. 2011; Sitarek & Bednarek 2012) and a declining seed photon density for inverse-Compton scattering (Dubus et al. 2010; Zdziarski et al. 2012). Detections prior to and after the quenched state would be due to the shock moving through this region as the jet turns off/on.

The application of the shock-in-jet model to Cyg X-3 strongly suggests that the faster, weaker radio flares (like in period I) occur closer to the core, whereas the brighter radio flares (like in period II) occur further downstream (Miller-Jones et al. 2009). A shock closer to the core during period I than during period II is also consistent with the brighter γ-ray emission that is observed in period I, assuming a jet with constant speed. The energy density in seed photons decreases if shocks occur far downstream, reducing the inverse-Compton luminosity in period II. An additional signature should be a stronger γ-ray modulation when shocks occur close to the core, hence close to the Wolf–Rayet companion star.

REFERENCES

Aleksić J. et al., 2010, ApJ, 721, 843

Atoyan A. M., Aharonian F. A., 1999, MNRAS, 302, 253

Atwood W. B. et al., 2009, ApJ, 697, 1071

Axelsson M., Larsson S., Hjalmarsdotter L., 2009, MNRAS, 394, 1544

Barthelmy S. D. et al., 2005, Space Sci. Rev., 120, 143

Bulgarelli A. et al., 2010, Astron. Telegram, 2645

Bulgarelli A. et al., 2011a, Astron. Telegram, 3141

Bulgarelli A. et al., 2011b, Astron. Telegram, 3151

Bulgarelli A. et al., 2011c, Astron. Telegram, 3239

Cerutti B., Dubus G., Malzac J., Szostek A., Belmont R., Zdziarski A. A., Henri G., 2011, A&A, 529, A120

Choudhury M., Rao A. R., Vadawale S. V., Jain A. K., Singh N. S., 2004, A&A, 420, 665

Coppi P. S., 1992, MNRAS, 258, 657

Coppi P. S., 1999, in Poutanen J., Svensson R., eds, ASP Conf. Ser. Vol. 161, High Energy Processes in Accreting Black Holes. Astron. Soc. Pac., San Francisco, p. 375

Corbel S., Hays E., 2010, Astron. Telegram, 2646

Corbel S. et al., 2011, Astron. Telegram, 3233

Dubus G., 2006, A&A, 456, 801

Dubus G., Cerutti B., Henri G., 2010, MNRAS, 404, L55

Fender R. P., Bell Burnell S. J., Waltman E. B., Pooley G. G., Ghigo F. D., Foster R. S., 1997, MNRAS, 288, 849

Fermi LAT Collaboration et al., 2009, Sci, 326, 1512 (FLC09)

Georganopoulos M., Aharonian F. A., Kirk J. G., 2002, A&A, 388, L25

Giacconi R., Gorenstein P., Gursky H., Waters J. R., 1967, ApJ, 148, L119

Gies D. R. et al., 2003, ApJ, 583, 424

Helene O., 1991, Nuclear Instruments and Methods in Physics Research A, 300, 132

Hjalmarsdotter L., Zdziarski A. A., Szostek A., Hannikainen D. C., 2009, MNRAS, 392, 251

Jahoda K., Markwardt C. B., Radeva Y., Rots A. H., Stark M. J., Swank J. H., Strohmayer T. E., Zhang W., 2006, ApJS, 163, 401

Koljonen K. I. I., Hannikainen D. C., McCollough M. L., Pooley G. G., Trushkin S. A., 2010, MNRAS, 406, 307

Kotani T. et al., 2011a, Astron. Telegram, 3130

Kotani T. et al., 2011b, Astron. Telegram, 3139

Leahy D. A., Darbro W., Elsner R. F., Weisskopf M. C., Kahn S., Sutherland P. G., Grindlay J. E., 1983, ApJ, 266, 160

Levine A. M., Bradt H., Cui W., Jernigan J. G., Morgan E. H., Remillard R., Shirey R. E., Smith D. A., 1996, ApJ, 469, L33

Lindfors E. J., Türler M., Hannikainen D. C., Pooley G., Tammi J., Trushkin S. A., Valtaoja E., 2007, A&A, 473, 923

Ling Z., Zhang S. N., Tang S., 2009, ApJ, 695, 1111

Matsuoka M. et al., 2009, PASJ, 61, 999

Mattox J. R. et al., 1996, ApJ, 461, 396

Miller-Jones J. C. A., Blundell K. M., Rupen M. P., Mioduszewski A. J., Duffy P., Beasley A. J., 2004, ApJ, 600, 368

Miller-Jones J. C. A., Rupen M. P., Türler M., Lindfors E. J., Blundell K. M., Pooley G. G., 2009, MNRAS, 394, 309

Mioduszewski A. J., Rupen M. P., Hjellming R. M., Pooley G. G., Waltman E. B., 2001, ApJ, 553, 766

Miyamoto S., Kimura K., Kitamoto S., Dotani T., Ebisawa K., 1991, ApJ, 383, 784

Newell S. J., Garrett M. A., Spencer R. E., 1998, MNRAS, 293, L17

Parsignault D. R. et al., 1972, Nat, 239, 123

Piano G., Bulgarelli A., Tavani M., Vittorini V., for the AGILE Team, McCollough M., Pooley G., Trushkin S., 2011a, 2011 Fermi Symp. Proc. - eConf C110509 (arXiv:1110.6043)

Piano G. et al., 2011b, Astron. Telegram, 3386

Richards J. L. et al., 2011, ApJS, 194, 29

Romero G. E., Torres D. F., Kaufman Bernadó M. M., Mirabel I. F., 2003, A&A, 410, L1

Sánchez-Sutil J. R., Martí J., Combi J. A., Luque-Escamilla P., Muñoz-Arjonilla A. J., Paredes J. M., Pooley G., 2008, A&A, 479, 523

Sitarek J., Bednarek W., 2012, MNRAS, in press (arXiv:1109.1978), (doi:10.1111/j.1365-2966.2012.20330.x)

Szostek A., Zdziarski A. A., 2008, MNRAS, 386, 593

Szostek A., Zdziarski A. A., McCollough M. L., 2008, MNRAS, 388, 1001

Tavani M. et al., 2009, Nat, 462, 620

Trushkin S., Bursov N. N., Nizhelskij N. A., Majorova E. K., Voitsik P. A., 2006, in Belloni, T., ed., VI Microquasar Workshop: Microquasars and Beyond. Proc. Science, http://pos.sissa.it/archive/conferences/033/015/MQW6_015.pdf

Tudose V. et al., 2010, MNRAS, 401, 890

van Kerkwijk M. H. et al., 1992, Nat, 355, 703

Waltman E. B., Fiedler R. L., Johnston K. L., Ghigo F. D., 1994, AJ, 108, 179

Waltman E. B., Ghigo F. D., Johnston K. J., Foster R. S., Fiedler R. L., Spencer J. H., 1995, AJ, 110, 290

Williams P. K. G. et al., 2011, ApJ, 733, L20

Zdziarski A. A., Sikora M., Dubus G., Yuan F., Cerutti B., Ogorzalek A., 2012, MNRAS, in press (arXiv:1111.0878) (doi:10.1111/j.1365-2966.2012.20519.x)

Zwart J. T. L. et al., 2008, MNRAS, 391, 1545

This paper has been typeset from a TEX/LATEX file prepared by the author.